Supplementary Material: Benchmark melting behavior of rhodium under megabar pressures

Jose Luis Rodrigo-Ramon[1*], Samuel R. Baty[4], Leonid Burakovsky[4], Pablo Botella[1], Anna Pakhomova[2], Egor Koemets[3], Bjorn Wehinger[2], Daniel Errandonea[1], Simone Anzellini[1]

[1*]Department of Applied Physics - Institute of Materials Science, Matter at High Pressure (MALTA) Consolider Team, University of Valencia, , Burjassot, Spain.

[2] European Synchrotron Radiation Facility, Grenoble, France.

[3] Diamond Light Source Ltd., Harwell Science and Innovation Campus, Didcot, Oxfordshire, UK.

[4] Theoretical Divisions, Los Alamos National Laboratory, Los Alamos, New Mexico, 87545 NM, United States of America.

*Corresponding author(s). E-mail(s): jose.l.rodrigo@uv.es;

1 HIGH TEMPERATURE LASER HEATING OF Rh

P_{MgO} (GPa)	T (K)	σ_T (K)	a_{Rh-fcc} (Å)	a_{MgO} (Å)	P_{MgO} (GPa)	T (K)	σ_T (K)	a_{Rh-fcc} (Å)	a_{MgO} (Å)
13(2)	1362	150	3.770(2)	4.162(2)	21(2)	1837	172	3.764(2)	4.127(2)
13(2)	1367	150	3.770(2)	4.163(2)	23(2)	1848	136	3.751(2)	4.114(2)
22(2)	1696	278	3.750(2)	4.115(2)	21(2)	1861	194	3.765(2)	4.127(2)
22(2)	1700	311	3.750(2)	4.115(2)	23(2)	1881	140	3.751(2)	4.114(2)
13(2)	1716	133	3.781(2)	4.176(2)	20(2)	1883	299	3.771(2)	4.133(2)
22(2)	1717	156	3.750(2)	4.115(2)	23(2)	1889	233	3.748(2)	4.113(2)
22(2)	1722	310	3.750(2)	4.115(2)	19(3)	1990	237	3.779(2)	4.144(2)
11(2)	1723	215	3.789(2)	4.193(2)	20(3)	2056	122	3.780(2)	4.143(2)
12(2)	1739	222	3.793(2)	4.187(2)	18(3)	2108	151	3.781(2)	4.156(2)
22(2)	1740	400	3.750(2)	4.115(2)	20(3)	2110	121	3.788(2)	4.145(2)
12(2)	1758	196	3.797(2)	4.185(2)	20(3)	2114	142	3.771(2)	4.144(2)
11(2)	1767	153	3.780(2)	4.196(2)	20(3)	2131	220	3.769(2)	4.143(2)
11(2)	1769	144	3.780(2)	4.196(2)	21(3)	2134	170	3.779(2)	4.142(2)
13(2)	1778	217	3.795(2)	4.183(2)	20(3)	2135	220	3.769(2)	4.146(2)
13(2)	1780	200	3.792(2)	4.183(2)	20(3)	2138	220	3.776(2)	4.146(2)
13(2)	1781	222	3.790(2)	4.179(2)	20(3)	2139	146	3.782(2)	4.143(2)
22(2)	1793	274	3.748(2)	4.027(2)	20(3)	2140	137	3.783(2)	4.144(2)
13(2)	1805	230	3.794(2)	4.179(2)	22(3)	2143	141	3.768(2)	4.135(2)
23(2)	1807	114	3.750(2)	4.115(2)	19(3)	2144	134	3.779(2)	4.154(2)
23(2)	1808	131	3.750(2)	4.115(2)	21(3)	2163	200	3.781(2)	4.142(2)
21(2)	1819	196	3.761(2)	4.126(2)	21(3)	2234	220	3.775(2)	4.147(2)
21(2)	1824	272	3.760(2)	4.123(2)	15(3)	2316	200	3.802(2)	4.194(2)
37(2)	1833	226	3.706(2)	4.034(2)	18(4)	2701	307	liquid	4.188(2)
37(2)	1834	230	3.706(2)	4.034(2)	16(3)	2500	250	liquid	4.198(2)
37(2)	1834	220	3.705(2)	4.033(2)	21(5)	3446	310	liquid	4.200(2)

Table S1: P–V–T data for Rh measured using MgO as the pressure-transmitting medium (PTM). a_{fcc} (Å) represents the measured lattice parameter of Rh. P_{MgO} corresponds to the pressure obtained from the MgO unit-cell parameter and the temperature measured using the thermal equation of state of MgO from [1]. T (K) and σ_T (K) denote the measured temperature and its uncertainty, respectively, obtained by spectral radiometry from the sample. Uncertainties in pressure and lattice parameters are given in parentheses for each measurement. For the lattice parameters we have evaluated an error of the order of 0.002 (Å) that agrees with the typical resolution associated with synchrotron XRD measurements.

P_{MgO} (GPa)	T (K)	σ_T (K)	a_{Rh-fcc} (Å)	a_{MgO} (Å)	P_{MgO} (GPa)	T (K)	σ_T (K)	a_{Rh-fcc} (Å)	a_{MgO} (Å)
21.0(1.1)	1284	162	3.746(2)	3.369(2)	20.0(1.8)	1876	255	3.760(2)	3.428(2)
22.0(1.2)	1360	135	3.745(2)	3.370(2)	39.0(1.8)	1877	244	3.692(2)	3.225(2)
21.0(1.2)	1382	124	3.747(2)	3.371(2)	46.0(1.8)	1880	200	3.685(2)	3.179(2)
58.0(1.2)	1386	261	3.630(2)	3.099(2)	34.0(1.8)	1883	123	3.709(2)	3.265(2)
58.0(1.2)	1403	208	3.630(2)	3.098(2)	39.0(1.8)	1883	330	3.690(2)	3.226(2)
57.0(1.2)	1404	240	3.636(2)	3.107(2)	39.0(1.8)	1896	106	3.692(2)	3.224(2)
57.0(1.2)	1405	250	3.636(2)	3.107(2)	92.0(1.8)	1902	133	3.571(2)	2.979(2)
34.0(1.3)	1430	190	3.697(2)	3.252(2)	39.0(1.8)	1904	188	3.692(2)	3.226(2)
39.0(1.3)	1431	112	3.681(2)	3.209(2)	39.0(1.8)	1905	112	3.692(2)	3.224(2)
34.0(1.3)	1439	163	3.697(2)	3.252(2)	37.0(1.8)	1907	133	3.693(2)	3.239(2)
59.0(1.3)	1447	250	3.631(2)	3.099(2)	60.0(1.8)	1908	196	3.635(2)	3.103(2)
39.0(1.3)	1448	131	3.681(2)	3.210(2)	20.0(1.8)	1913	236	3.762(2)	3.430(2)
39.0(1.3)	1452	175	3.680(2)	3.209(2)	63.0(1.8)	1914	165	3.628(2)	3.087(2)
34.0(1.3)	1452	132	3.697(2)	3.253(2)	36.0(1.8)	1919	221	3.695(2)	3.248(2)
91.0(1.3)	1454	114	3.565(2)	2.977(2)	39.0(1.8)	1921	141	3.698(2)	3.225(2)
21.0(1.3)	1456	150	3.754(2)	3.381(2)	39.0(1.8)	1926	103	3.693(2)	3.224(2)
41.0(1.3)	1459	211	3.678(2)	3.197(2)	20.0(1.8)	1932	129	3.764(2)	3.433(2)
38.0(1.3)	1462	225	3.686(2)	3.221(2)	26.0(1.8)	1936	264	3.724(2)	3.343(2)
38.0(1.3)	1464	249	3.687(2)	3.221(2)	58.0(1.8)	1936	202	3.646(2)	3.114(2)
41.0(1.3)	1467	190	3.677(2)	3.196(2)	92.0(1.8)	1936	116	3.570(2)	2.981(2)
50.0(1.3)	1468	170	3.655(2)	3.144(2)	89.0(1.8)	1942	140	3.581(2)	2.990(2)
50.0(1.3)	1470	130	3.657(2)	3.145(2)	34.0(1.8)	1949	134	3.714(2)	3.267(2)
38.0(1.3)	1473	227	3.686(2)	3.221(2)	41.0(1.8)	1949	192	3.696(2)	3.211(2)
21.0(1.3)	1476	161	3.745(2)	3.381(2)	39.0(1.8)	1951	325	3.692(2)	3.227(2)
61.0(1.3)	1478	190	3.626(2)	3.087(2)	36.0(1.9)	1955	221	3.699(2)	3.251(2)
38.0(1.3)	1478	260	3.686(2)	3.221(2)	63.0(1.9)	1955	150	3.626(2)	3.090(2)
44.0(1.3)	1479	160	3.677(2)	3.176(2)	39.0(1.9)	1959	112	3.693(2)	3.225(2)
60.0(1.3)	1485	150	3.626(2)	3.094(2)	26.0(1.9)	1966	263	3.723(2)	3.344(2)
21.0(1.3)	1488	147	3.749(2)	3.384(2)	92.0(1.9)	1966	115	3.569(2)	2.981(2)
38.0(1.3)	1492	250	3.685(2)	3.220(2)	37.0(1.9)	1972	168	3.693(2)	3.241(2)
38.0(1.3)	1494	197	3.686(2)	3.220(2)	26.0(1.9)	1973	233	3.726(2)	3.345(2)
44.0(1.3)	1499	150	3.675(2)	3.177(2)	46.0(1.9)	1977	200	3.688(2)	3.181(2)
38.0(1.3)	1501	250	3.685(2)	3.219(2)	93.0(1.9)	1978	140	3.568(2)	2.979(2)
34.0(1.3)	1501	142	3.697(2)	3.253(2)	39.0(1.9)	1978	280	3.694(2)	3.228(2)
91.0(1.3)	1505	170	3.567(2)	2.977(2)	60.0(1.9)	1981	204	3.642(2)	3.105(2)
50.0(1.4)	1507	170	3.659(2)	3.146(2)	50.0(1.9)	1985	153	3.665(2)	3.156(2)
38.0(1.4)	1510	286	3.685(2)	3.219(2)	36.0(1.9)	1991	221	3.697(2)	3.249(2)
41.0(1.4)	1513	180	3.679(2)	3.199(2)	41.0(1.9)	1994	257	3.679(2)	3.212(2)
44.0(1.4)	1514	150	3.675(2)	3.177(2)	40.0(1.9)	1996	165	3.699(2)	3.223(2)
63.0(1.4)	1516	216	3.621(2)	3.081(2)	26.0(1.9)	1997	251	3.723(2)	3.345(2)
19.0(1.4)	1524	181	3.750(2)	3.406(2)	39.0(1.9)	2004	163	3.694(2)	3.228(2)
38.0(1.4)	1532	275	3.685(2)	3.220(2)	38.0(1.9)	2016	194	3.688(2)	3.239(2)

38.0(1.4)	1532	270	3.685(2)	3.220(2)	40.0(1.9)	2026	148	3.696(2)	3.220(2)
38.0(1.4)	1533	216	3.685(2)	3.220(2)	36.0(1.9)	2026	221	3.699(2)	3.250(2)
88.0(1.4)	1539	180	3.577(2)	2.989(2)	39.0(1.9)	2027	285	3.694(2)	3.229(2)
59.0(1.4)	1539	215	3.632(2)	3.099(2)	34.0(1.9)	2027	155	3.718(2)	3.269(2)
21.0(1.4)	1545	115	3.750(2)	3.392(2)	39.0(1.9)	2028	160	3.695(2)	3.230(2)
50.0(1.4)	1546	152	3.659(2)	3.146(2)	89.0(1.9)	2030	184	3.582(2)	2.990(2)
65.0(1.4)	1546	150	3.615(2)	3.074(2)	61.0(1.9)	2031	170	3.637(2)	3.100(2)
38.0(1.4)	1547	247	3.688(2)	3.223(2)	26.0(1.9)	2034	232	3.730(2)	3.348(2)
45.0(1.4)	1549	135	3.678(2)	3.177(2)	37(2)	2045	160	3.693(2)	3.242(2)
34.0(1.4)	1551	134	3.697(2)	3.255(2)	37(2)	2048	221	3.697(2)	3.250(2)
39.0(1.4)	1552	113	3.687(2)	3.212(2)	42(2)	2053	200	3.697(2)	3.209(2)
60.0(1.4)	1555	150	3.625(2)	3.094(2)	62(2)	2075	93	3.639(2)	3.094(2)
50.0(1.4)	1555	200	3.652(2)	3.143(2)	50(2)	2079	200	3.665(2)	3.158(2)
41.0(1.4)	1557	191	3.680(2)	3.201(2)	27(2)	2087	211	3.729(2)	3.348(2)
60.0(1.4)	1571	150	3.627(2)	3.094(2)	60(2)	2090	211	3.643(2)	3.107(2)
57.0(1.4)	1572	200	3.637(2)	3.108(2)	37(2)	2092	200	3.699(2)	3.252(2)
21.0(1.4)	1578	150	3.756(2)	3.385(2)	39(2)	2093	165	3.698(2)	3.229(2)
63.0(1.4)	1578	176	3.623(2)	3.082(2)	41(2)	2105	165	3.700(2)	3.219(2)
34.0(1.4)	1588	126	3.698(2)	3.257(2)	93(2)	2105	147	3.570(2)	2.981(2)
91.0(1.4)	1593	151	3.566(2)	2.978(2)	62(2)	2107	200	3.633(2)	3.095(2)
65.0(1.4)	1593	150	3.615(2)	3.074(2)	39(2)	2107	195	3.697(2)	3.231(2)
38.0(1.5)	1602	172	3.689(2)	3.223(2)	39(2)	2111	245	3.692(2)	3.230(2)
89.0(1.5)	1611	110	3.576(2)	2.986(2)	62(2)	2113	162	3.640(2)	3.095(2)
44.0(1.5)	1615	186	3.672(2)	3.183(2)	20(2)	2129	122	3.773(2)	3.439(2)
50.0(1.5)	1617	170	3.659(2)	3.148(2)	27(2)	2131	211	3.730(2)	3.349(2)
65.0(1.5)	1617	162	3.616(2)	3.074(2)	37(2)	2144	200	3.699(2)	3.254(2)
45.0(1.5)	1627	190	3.680(2)	3.177(2)	36(2)	2154	353	3.699(2)	3.257(2)
38.0(1.5)	1628	142	3.689(2)	3.223(2)	63(2)	2177	196	3.638(2)	3.094(2)
60.0(1.5)	1630	133	3.628(2)	3.094(2)	38(2)	2178	170	3.694(2)	3.246(2)
38.0(1.5)	1640	124	3.689(2)	3.224(2)	58(2)	2182	300	3.648(2)	3.118(2)
91.0(1.5)	1641	130	3.571(2)	2.978(2)	37(2)	2189	200	3.700(2)	3.254(2)
21.0(1.5)	1649	150	3.759(2)	3.388(2)	39(2)	2194	231	3.698(2)	3.236(2)
41.0(1.5)	1651	199	3.682(2)	3.204(2)	33(2)	2203	171	3.722(2)	3.284(2)
38.0(1.5)	1651	202	3.689(2)	3.223(2)	61(2)	2240	250	3.635(2)	3.103(2)
34.0(1.5)	1660	132	3.698(2)	3.258(2)	63(2)	2246	250	3.638(2)	3.096(2)
38.0(1.5)	1660	189	3.688(2)	3.223(2)	27(2)	2256	211	3.737(2)	3.352(2)
59.0(1.5)	1660	152	3.635(2)	3.100(2)	27(2)	2275	211	3.719(2)	3.351(2)
45.0(1.5)	1662	280	3.674(2)	3.179(2)	27(2)	2288	211	3.733(2)	3.354(2)
89.0(1.5)	1666	120	3.576(2)	2.986(2)	93(2)	2295	96.9	3.573(2)	2.984(2)
22.0(1.5)	1669	163	3.756(2)	3.384(2)	27(2)	2299	211	3.737(2)	3.353(2)
50.0(1.5)	1681	150	3.659(2)	3.150(2)	60(2)	2318	247	3.646(2)	3.110(2)
38.0(1.5)	1683	119	3.689(2)	3.223(2)	37(2)	2325	163	3.697(2)	3.254(2)
40.0(1.5)	1684	126	3.692(2)	3.215(2)	63(2)	2328	200	3.633(2)	3.098(2)
34.0(1.6)	1687	104	3.698(2)	3.259(2)	27(2)	2331	211	3.733(2)	3.354(2)
34.0(1.6)	1700	117	3.697(2)	3.259(2)	36(2)	2332	212	3.702(2)	3.262(2)

65.0(1.6)	1700	160	3.617(2)	3.075(2)	64(2)	2335	414	3.637(2)	3.092(2)
38.0(1.6)	1705	130	3.689(2)	3.224(2)	27(2)	2335	211	3.737(2)	3.354(2)
92.0(1.6)	1709	128	3.570(2)	2.978(2)	27(2)	2336	211	3.735(2)	3.354(2)
63.0(1.6)	1710	169	3.625(2)	3.083(2)	63(2)	2345	300	3.636(2)	3.096(2)
45.0(1.6)	1712	140	3.684(2)	3.178(2)	27(2)	2346	211	3.735(2)	3.355(2)
62.0(1.6)	1712	90	3.629(2)	3.089(2)	50(2)	2355	200	3.667(2)	3.163(2)
59.0(1.6)	1722	164	3.635(2)	3.101(2)	62(2)	2360	150	3.637(2)	3.103(2)
22.0(1.6)	1731	169	3.760(2)	3.385(2)	27(2)	2363	211	3.735(2)	3.355(2)
22.0(1.6)	1732	150	3.762(2)	3.390(2)	40(2)	2374	200	3.700(2)	3.237(2)
34.0(1.6)	1747	120	3.700(2)	3.260(2)	64(2)	2388	207	3.634(2)	3.093(2)
89.0(1.6)	1748	140	3.580(2)	2.990(2)	90(2)	2399	178	3.582(2)	2.994(2)
50.0(1.6)	1761	160	3.660(2)	3.150(2)	31(2)	2411	150	3.724(2)	3.313(2)
34.0(1.6)	1761	147	3.700(2)	3.260(2)	94(2)	2413	200	3.571(2)	2.982(2)
92.0(1.6)	1764	150	3.570(2)	2.980(2)	40(2)	2416	325	3.702(2)	3.236(2)
38.0(1.6)	1765	244	3.690(2)	3.230(2)	36(2)	2420	230	3.706(2)	3.266(2)
36.0(1.6)	1765	221	3.690(2)	3.240(2)	42(2)	2441	195	3.702(2)	3.223(2)
41.0(1.6)	1766	215	3.690(2)	3.210(2)	37(2)	2450	216	3.702(2)	3.265(2)
92.0(1.6)	1770	140	3.570(2)	2.980(2)	40(2)	2461	200	3.699(2)	3.236(2)
36.0(1.7)	1773	221	3.690(2)	3.250(2)	40(2)	2461	167	3.701(2)	3.239(2)
26.0(1.7)	1789	226	3.720(2)	3.340(2)	41(3)	2496	299	3.704(2)	3.235(2)
26.0(1.7)	1790	127	3.720(2)	3.340(2)	60(3)	2505	300	3.649(2)	3.114(2)
26.0(1.7)	1791	230	3.720(2)	3.340(2)	51(3)	2515	243	3.678(2)	3.166(2)
39.0(1.7)	1795	128	3.690(2)	3.230(2)	62(3)	2553	200	3.633(2)	3.104(2)
26.0(1.7)	1796	131	3.720(2)	3.340(2)	41(3)	2558	185	3.704(2)	3.230(2)
38.0(1.7)	1798	160	3.690(2)	3.230(2)	58(3)	2570	352	3.653(2)	3.127(2)
26.0(1.7)	1799	134	3.720(2)	3.340(2)	47(3)	2576	230	3.687(2)	3.189(2)
60.0(1.7)	1799	170	3.640(2)	3.100(2)	61(3)	2583	272	3.651(2)	3.114(2)
39.0(1.7)	1799	139	3.690(2)	3.230(2)	35(3)	2635	223	3.732(2)	3.282(2)
36.0(1.7)	1800	221	3.690(2)	3.240(2)	42(3)	2636	200	3.705(2)	3.226(2)
39.0(1.7)	1801	124	3.690(2)	3.230(2)	51(3)	2645	260	3.669(2)	3.167(2)
39.0(1.7)	1801	127	3.690(2)	3.230(2)	47(3)	2685	220	3.692(2)	3.193(2)
41.0(1.7)	1802	477	3.680(2)	3.210(2)	66(3)	2694	200	3.627(2)	3.090(2)
41.0(1.7)	1803	432	3.680(2)	3.210(2)	58(3)	2705	297	3.654(2)	3.129(2)
39.0(1.7)	1803	146	3.690(2)	3.230(2)	60(3)	2728	300	3.652(2)	3.118(2)
38.0(1.7)	1804	113	3.691(2)	3.234(2)	92(3)	2737	171	3.574(2)	2.992(2)
37.0(1.7)	1805	114	3.691(2)	3.234(2)	93(3)	2737	159	3.576(2)	2.987(2)
41.0(1.7)	1806	268	3.677(2)	3.207(2)	93(3)	2750	69.6	3.583(2)	2.989(2)
38.0(1.7)	1807	137	3.690(2)	3.233(2)	38(3)	2786	200	3.704(2)	3.270(2)
26.0(1.7)	1808	139	3.725(2)	3.340(2)	68(3)	2786	182	3.630(2)	3.084(2)
38.0(1.7)	1808	138	3.690(2)	3.234(2)	41(3)	2793	269	3.702(2)	3.239(2)
26.0(1.7)	1811	158	3.725(2)	3.340(2)	40(3)	2810	300	3.704(2)	3.246(2)
41.0(1.7)	1811	256	3.677(2)	3.207(2)	36(3)	2817	285	3.734(2)	3.286(2)
39.0(1.7)	1811	121	3.688(2)	3.226(2)	93(3)	2862	288	3.582(2)	2.992(2)
26.0(1.7)	1811	139	3.720(2)	3.341(2)	93(3)	2880	227	3.576(2)	2.990(2)
41.0(1.7)	1813	392	3.678(2)	3.207(2)	57(3)	2882	340	3.652(2)	3.139(2)

39.0(1.7)	1813	166	3.691(2)	3.225(2)	52(3)	2917	51	3.694(2)	3.172(2)
38.0(1.7)	1814	128	3.689(2)	3.232(2)	93(3)	2918	250	3.578(2)	2.991(2)
37.0(1.7)	1815	155	3.691(2)	3.235(2)	90(3)	2919	204	3.588(2)	3.002(2)
38.0(1.7)	1818	117	3.688(2)	3.227(2)	94(3)	2952	250	3.572(2)	2.990(2)
38.0(1.7)	1818	137	3.689(2)	3.232(2)	41(3)	2960	267	3.700(2)	3.252(2)
41.0(1.7)	1819	290	3.677(2)	3.207(2)	93(3)	3007	325	3.586(2)	2.994(2)
37.0(1.7)	1820	149	3.692(2)	3.236(2)	63(3)	3023	250	3.635(2)	3.109(2)
34.0(1.7)	1820	133	3.709(2)	3.264(2)	41(3)	3053	270	3.707(2)	3.253(2)
37.0(1.7)	1820	148	3.691(2)	3.235(2)	62(3)	3059	655	3.646(2)	3.119(2)
38.0(1.7)	1822	135	3.689(2)	3.232(2)	42(3)	3059	220	3.708(2)	3.245(2)
38.0(1.7)	1823	146	3.688(2)	3.231(2)	43(3)	3074	215	3.705(2)	3.237(2)
38.0(1.7)	1824	145	3.689(2)	3.231(2)	95(3)	3113	306	3.584(2)	2.988(2)
38.0(1.7)	1825	146	3.688(2)	3.230(2)	41(3)	3120	232	3.708(2)	3.252(2)
26.0(1.7)	1825	382	3.721(2)	3.342(2)	60(3)	3124	468	3.658(2)	3.127(2)
36.0(1.7)	1829	221	3.688(2)	3.244(2)	93(3)	3148	300	3.577(2)	2.994(2)
38.0(1.7)	1830	139	3.688(2)	3.229(2)	95(3)	3153	380	3.574(2)	2.989(2)
37.0(1.7)	1831	256	3.683(2)	3.235(2)	95(3)	3199	741	3.580(2)	2.988(2)
37.0(1.7)	1832	221	3.685(2)	3.236(2)	92(3)	3203	300	3.589(2)	2.997(2)
38.0(1.7)	1833	140	3.687(2)	3.228(2)	94(3)	3216	383	3.588(2)	2.993(2)
37.0(1.7)	1833	254	3.685(2)	3.237(2)	94(3)	3228	438	3.575(2)	2.991(2)
37.0(1.7)	1833	287	3.685(2)	3.237(2)	41(3)	3241	236	3.706(2)	3.256(2)
26.0(1.7)	1834	164	3.726(2)	3.341(2)	95(3)	3242	291	3.590(2)	2.990(2)
92.0(1.7)	1837	135	3.571(2)	2.979(2)	94(3)	3300	230	3.598(2)	2.994(2)
36.0(1.7)	1838	221	3.692(2)	3.246(2)	94(3)	3317	428	3.590(2)	2.993(2)
58.0(1.7)	1838	222	3.641(2)	3.112(2)	94(3)	3318	300	3.588(2)	2.994(2)
22.0(1.7)	1838	172	3.767(2)	3.397(2)	91(3)	3324	230	3.590(2)	3.003(2)
41.0(1.7)	1839	385	3.677(2)	3.208(2)	66(3)	3381	200	3.639(2)	3.104(2)
37.0(1.7)	1840	221	3.685(2)	3.238(2)	93(4)	3914	444	3.600(2)	3.006(2)
37.0(1.7)	1842	221	3.685(2)	3.238(2)	94(4)	3969	220	3.596(2)	3.005(2)
39.0(1.7)	1842	116	3.692(2)	3.225(2)	94(4)	4013	337	3.591(2)	3.003(2)
36.0(1.7)	1843	221	3.687(2)	3.244(2)	93(4)	4053	400	3.587(2)	3.007(2)
37.0(1.7)	1847	221	3.685(2)	3.239(2)	96(4)	4150	296	3.597(2)	3.000(2)
36.0(1.7)	1847	221	3.692(2)	3.246(2)	95(4)	4250	654	3.579(2)	3.004(2)
37.0(1.7)	1848	221	3.685(2)	3.238(2)	93(5)	4386	450	3.591(2)	3.012(2)
39.0(1.7)	1849	144	3.698(2)	3.227(2)	60(4)	3765	500	liquid	3.105(2)
26.0(1.7)	1850	140	3.723(2)	3.341(2)	41(3)	3247	261	liquid	3.208(2)
37.0(1.7)	1852	221	3.685(2)	3.239(2)	41(3)	3182	304	liquid	3.209(2)
37.0(1.7)	1854	221	3.686(2)	3.240(2)	65(4)	3851	200	liquid	3.086(2)
39.0(1.7)	1857	232	3.688(2)	3.226(2)	20(3)	2600	190	liquid	3.397(2)
89.0(1.8)	1863	140	3.580(2)	2.989(2)	24(3)	2741	234	liquid	3.350(2)
41.0(1.8)	1864	195	3.694(2)	3.209(2)	33(3)	3182	200	liquid	3.264(2)
26.0(1.8)	1866	142	3.724(2)	3.341(2)	37(3)	3146	260	liquid	3.238(2)
22.0(1.8)	1866	150	3.767(2)	3.391(2)	43(3)	3218	372	liquid	3.192(2)
50.0(1.8)	1868	126	3.663(2)	3.153(2)	97(5)	4700	500	liquid	2.977(2)
39.0(1.8)	1869	100	3.692(2)	3.223(2)	98(6)	5312	297	liquid	2.977(2)

41.0(1.8)	1876	352	3.678(2)	3.209(2)	94(5)	5043	522	liquid	2.987(2)
37.0(1.8)	1876	172	3.692(2)	3.237(2)					

Table S2: P–V–T data for Rh measured using KCl as the pressure-transmitting medium (PTM). a_{fcc} (Å) represents the measured lattice parameter of Rh. $\mathrm{P_{KCl}}$ corresponds to the pressure obtained from the KCl unit-cell parameter B2 phase and the temperature measured using the thermal equation of state of MgO from [1]. T (K) and σ_T (K) denote the measured temperature and its uncertainty, respectively, obtained by spectral radiometry from the sample. Uncertainties in pressure and lattice parameters are given in parentheses for each measurement. For the lattice parameters we have evaluated an error of the order of 0.002 (Å) that agrees with the typical resolution associated with synchrotron XRD measurements.

2 CALCULATED EOS ISOTHERMS FOR Rh

298 K		800 K		2000 K		3000 K		4000 K	
P(GPa)	V(Å)	P(GPa)	V(Å)	P(GPa)	V(Å)	P(GPa)	V(Å)	P(GPa)	V(Å)
-0.15126	55.134	-5.2776	57.13	-5.2776	59.703	-5.2776	62.74	-5.2776	68.361
0.9754	54.889	-4.0383	56.788	-4.0383	59.234	-4.0383	62.044	-4.0383	66.793
2.1021	54.651	-2.7989	56.46	-2.7989	58.791	-2.7989	61.41	-2.7989	65.561
3.2287	54.42	-1.5596	56.145	-1.5596	58.372	-1.5596	60.826	-1.5596	64.532
4.3554	54.195	-0.32026	55.842	-0.32026	57.974	-0.32026	60.284	-0.32026	63.644
6.6087	53.763	2.1584	55.267	2.1584	57.233	2.1584	59.304	2.1584	62.15
7.7354	53.556	3.3977	54.994	3.3977	56.887	3.3977	58.857	3.3977	61.507
8.862	53.353	4.6371	54.729	4.6371	56.555	4.6371	58.435	4.6371	60.915
9.9887	53.155	5.8764	54.473	5.8764	56.236	5.8764	58.034	5.8764	60.367
13.369	52.587	9.5944	53.749	9.5944	55.349	9.5944	56.939	9.5944	58.927
14.495	52.406	10.834	53.521	10.834	55.073	10.834	56.605	10.834	58.5
17.875	51.886	14.552	52.872	14.552	54.297	14.552	55.679	14.552	57.345
19.002	51.719	15.791	52.667	15.791	54.054	15.791	55.392	15.791	56.994
20.129	51.556	17.03	52.466	17.03	53.817	17.03	55.115	17.03	56.658
22.382	51.238	19.509	52.079	19.509	53.364	19.509	54.587	19.509	56.024
23.509	51.084	20.748	51.891	20.748	53.146	20.748	54.335	20.748	55.725
24.635	50.932	21.988	51.708	21.988	52.934	21.988	54.091	21.988	55.437
26.889	50.637	24.466	51.353	24.466	52.524	24.466	53.623	24.466	54.889
28.015	50.493	25.706	51.181	25.706	52.327	25.706	53.398	25.706	54.628
29.142	50.351	26.945	51.013	26.945	52.134	26.945	53.179	26.945	54.375
30.269	50.212	28.184	50.847	28.184	51.946	28.184	52.966	28.184	54.129
32.522	49.941	30.663	50.526	30.663	51.581	30.663	52.555	30.663	53.659
33.649	49.808	31.902	50.37	31.902	51.404	31.902	52.357	31.902	53.433
34.775	49.677	33.142	50.217	33.142	51.231	33.142	52.164	33.142	53.214
37.029	49.422	35.62	49.918	35.62	50.895	35.62	51.79	35.62	52.791
39.282	49.174	38.099	49.63	38.099	50.573	38.099	51.431	38.099	52.388
40.409	49.053	39.338	49.489	39.338	50.416	39.338	51.258	39.338	52.194
42.662	48.815	41.817	49.215	41.817	50.11	41.817	50.921	41.817	51.819
43.789	48.699	43.056	49.081	43.056	49.961	43.056	50.757	43.056	51.637
44.915	48.584	44.296	48.949	44.296	49.815	44.296	50.597	44.296	51.459
46.042	48.471	45.535	48.819	45.535	49.672	45.535	50.44	45.535	51.285
47.169	48.36	46.774	48.691	46.774	49.53	46.774	50.285	46.774	51.114
48.295	48.249	48.014	48.565	48.014	49.391	48.014	50.133	48.014	50.947
49.422	48.141	49.253	48.441	49.253	49.255	49.253	49.984	49.253	50.783
50.549	48.033	50.492	48.319	50.492	49.12	50.492	49.838	50.492	50.622
52.802	47.822	52.971	48.079	52.971	48.857	52.971	49.552	52.971	50.309
53.929	47.719	54.21	47.962	54.21	48.729	54.21	49.413	54.21	50.157
56.182	47.515	56.689	47.732	56.689	48.477	56.689	49.141	56.689	49.861
57.309	47.415	57.928	47.62	57.928	48.355	57.928	49.008	57.928	49.716
58.435	47.317	59.168	47.509	59.168	48.233	59.168	48.877	59.168	49.574
59.562	47.219	60.407	47.399	60.407	48.114	60.407	48.748	60.407	49.435

60.689	47.123	61.646	47.291	61.646	47.996	61.646	48.622	61.646	49.297
62.942	46.933	64.125	47.078	64.125	47.766	64.125	48.373	64.125	49.029
64.069	46.84	65.364	46.974	65.364	47.653	65.364	48.252	65.364	48.898
66.322	46.656	67.843	46.769	67.843	47.431	67.843	48.014	67.843	48.642
67.449	46.566	69.082	46.668	69.082	47.322	69.082	47.898	69.082	48.516
68.575	46.477	70.322	46.569	70.322	47.215	70.322	47.783	70.322	48.393
69.702	46.388	71.561	46.471	71.561	47.109	71.561	47.67	71.561	48.271
70.829	46.301	72.8	46.374	72.8	47.004	72.8	47.558	72.8	48.151
73.082	46.129	75.279	46.183	75.279	46.799	75.279	47.339	75.279	47.916
74.209	46.044	76.518	46.089	76.518	46.698	76.518	47.231	76.518	47.801
76.462	45.876	78.997	45.904	78.997	46.499	78.997	47.02	78.997	47.576
78.715	45.713	81.475	45.723	81.475	46.306	81.475	46.814	81.475	47.356
79.842	45.632	82.715	45.634	82.715	46.21	82.715	46.713	82.715	47.248
80.968	45.552	83.954	45.546	83.954	46.116	83.954	46.613	83.954	47.142
82.095	45.472	85.193	45.459	85.193	46.023	85.193	46.515	85.193	47.037
83.222	45.394	86.433	45.373	86.433	45.931	86.433	46.417	86.433	46.933
84.348	45.316	87.672	45.288	87.672	45.84	87.672	46.32	87.672	46.831
86.602	45.163	90.151	45.119	90.151	45.66	90.151	46.131	90.151	46.629
87.728	45.087	91.39	45.037	91.39	45.572	91.39	46.037	91.39	46.53
89.982	44.937	93.869	44.873	93.869	45.398	93.869	45.854	93.869	46.336
92.235	44.791	96.347	44.713	96.347	45.228	96.347	45.674	96.347	46.146
93.362	44.718	97.587	44.634	97.587	45.144	97.587	45.586	97.587	46.052
94.488	44.646	98.826	44.556	98.826	45.061	98.826	45.498	98.826	45.96
96.742	44.504	101.3	44.402	101.3	44.897	101.3	45.326	101.3	45.778
97.868	44.434	102.54	44.326	102.54	44.816	102.54	45.241	102.54	45.688
98.995	44.365	103.78	44.25	103.78	44.737	103.78	45.157	103.78	45.6
100.12	44.296	105.02	44.176	105.02	44.657	105.02	45.074	105.02	45.512
103.5	44.093	108.74	43.955	108.74	44.424	108.74	44.829	108.74	45.254
104.63	44.026	109.98	43.883	109.98	44.348	109.98	44.749	109.98	45.17
105.76	43.96	111.22	43.812	111.22	44.272	111.22	44.67	111.22	45.087
106.88	43.894	112.46	43.741	112.46	44.197	112.46	44.591	112.46	45.004

Table S3: The unit-cell volume (Å^3) of fcc Rh along several isotherms between 0–112 GPa was calculated using the fitted thermal equation of state (EoS) determined in this study, with parameters $V_0 = 55.100(14)$ Å^3, $K_0 = 251(2)$ GPa, $K_0' = 5.69(8)$, and $\alpha_0 = 2.28(4) \times 10^{-5}$ K^{-1}. It should be noted that some of the reported volumes correspond to liquid Rh, as indicated by the melting line and melting point calculations presented in this work. Specifically, for the 3000 K isotherm, data points at pressures below approximately 28.6 GPa correspond to liquid Rh. Likewise, for the 4000 K isotherm, volumes reported at pressures below 73.7 GPa also correspond to the liquid phase.

3 CHEMICAL REACTION DURING LASER HEATING

In situ X-ray diagnostic of laser heating allows following, in real time, the transformations in the sample. These transformations include chemical reaction with its environment. We have observed a chemical reaction between rhodium and carbon migrating from diamond anvils, resulting in the formation of Rh_2C [2]. The chemical reaction was only observed with the use of KCl as PTM and was observed at temperature higher than the melting temperature of KCl. Peaks assigned to Rh_2C were detecetd after the diffuse signal coming from liquid KCl was observed (see top of figure S1).

The additional peaks highlighted in Fig. S1 (orange circles and arrows) are interpreted as arising from the formation of Rh_2C. These peaks are consistent with an orthorhombic *Pmnn* structure with unit-cell parameters $a = 2.872$ Å, $b = 4.374$ Å, and $c = 4.355$ Å. This structure has been previously reported for Rh_2C at ambient conditions. Considering the experimental conditions (∼65 GPa and temperatures up to ∼4000 K), the extracted unit-cell parameters are in reasonable agreement with those reported at ambient pressure [2].

The most plausible explanation for the formation of Rh_2C is that upon melting of the KCl pressure-transmitting medium, carbon diffusion from diamods likely occurred, leading to carbide formation under high P–T conditions. Notably, this phenomenon was observed in only one heating ramp, and the amount of Rh_2C formed is limited, as evidenced in Fig.S1, especially when compared with more extensive carbide formation reported in other systems (e.g., TaC [3]).

This interpretation is further supported by the temperature evolution during the sequence of diffraction frames in which Rh_2C appears. In the first four frames, temperatures reach ∼6000 K. In frame 5, the temperature decreases to ∼4500 K, at which point the first diffraction peaks attributable to Rh_2C become visible (see corresponding integrated patterns and diffraction images). In subsequent frames, a further drop in temperature to ∼3000 K is observed, accompanied by the appearance of additional peaks associated with Rh_2C formation. These abrupt temperature drops may be linked to experimental instabilities, such as carbon diffusion processes or motion of molten KCl , both of which could perturb the heating conditions.

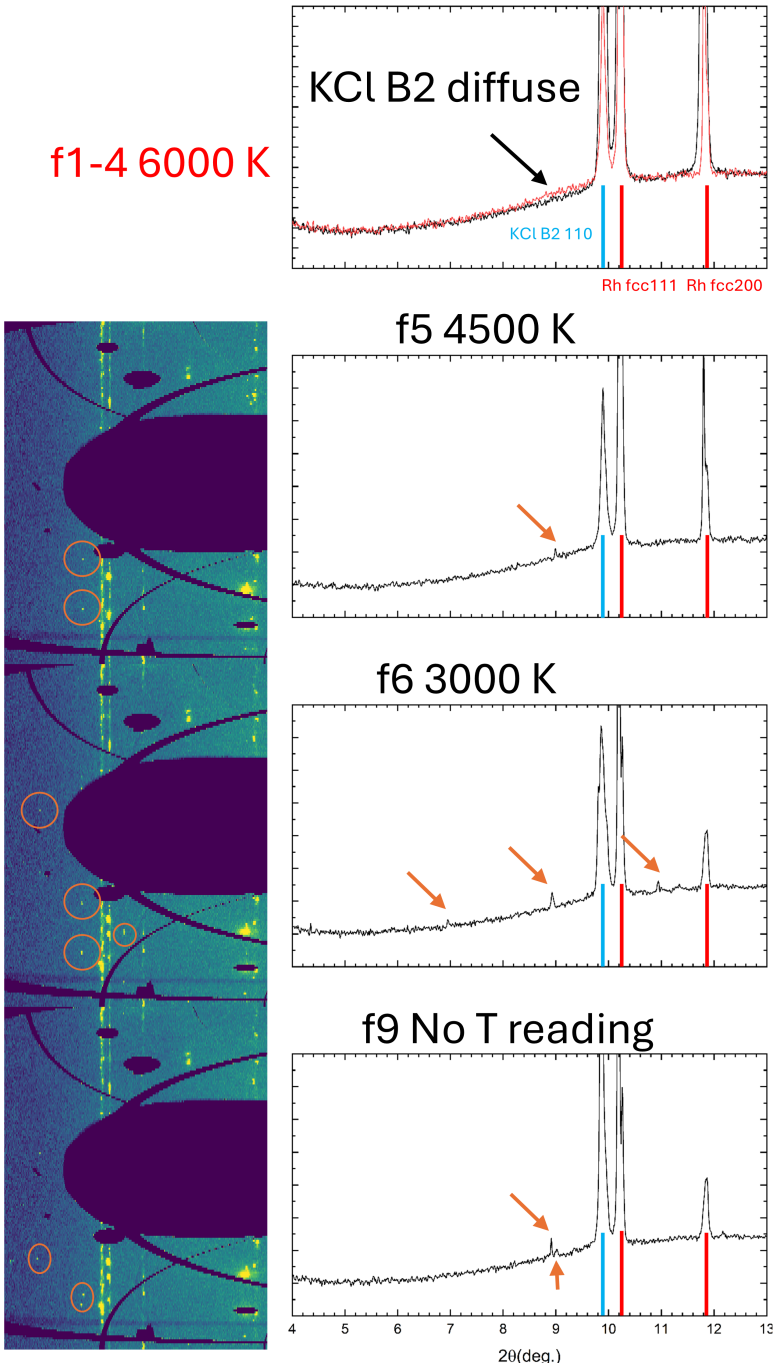

Figure S1 Azimuthally unwrapped X-ray diffraction images (left) and integrated images (right) for selected heating steps where a reaction was identified. Bragg reflections for KCl and Rh are indicated by blue and red lines, respectively, while orange circles and arrows highlight the appearance of new single-crystal reflections associated with the formation of rhodium carbide (Rh_2C).

4 MICROSTRUCTURAL ANALYSIS

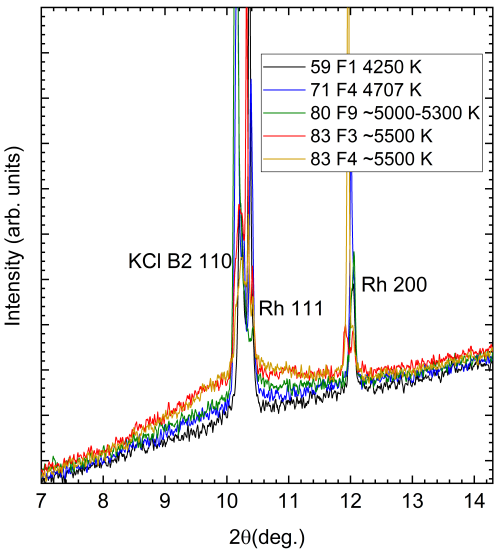

Figure S2 Integrated XRD patterns collected upon increasing temperature at approximately 100 GPa. At 4250 K (black pattern), Rh remains in the solid phase. The onset of melting is observed at 4700 K (blue pattern). At higher temperatures (5000–5300K, green pattern), a clear increase in the diffuse signal is observed, indicating a larger fraction of liquid Rh. At even higher temperatures (5500K, red and yellow patterns), the diffuse scattering further increases, possibly reflecting the presence of a mixed liquid/solid KCl phase in addition to the Rh .

At very high pressures (∼100 GPa), diffuse scattering is also observed. However, due to the proximity of the Bragg reflections (110) of KCl-B2 and (111) of *fcc* Rh, further analysis is required for unambiguous identification of the diffuse scattering origin. Figure S2 shows selected diffuse scattering patterns collected around 100 GPa. The close spacing of these Bragg peaks complicates the determination of the origin of the diffuse halo, as also reported in other studies[4].

A first analysis suggests that the initial diffuse signal corresponds to rhodium, as it is bounded toward its Bragg peak (blue and green lines in Fig.S2), indicating a melting locus around 4700-5000 K. Furthermore, examining the evolution of the diffuse halo with increasing temperature (yellow and red lines in Fig.S2) shows a more pronounced growth on the left side, near the KCl-B2 (110) reflection. This behavior suggests that at higher temperatures (∼5500 K), KCl also melts, in agreement with the proposed melting line.

As discussed by Hrubiak *et al.*[5], melting can be identified by tracking microstructural changes in grain size in rapidly quenched samples in the LH-DAC. Therefore, microstructural analysis provides a reliable criterion for detecting melting, provided that the quenching rate is sufficiently fast. In this study, we employed this approach as an additional method for melt detection, complementing the identification based on diffuse scattering, which itself is a robust indicator of melting.

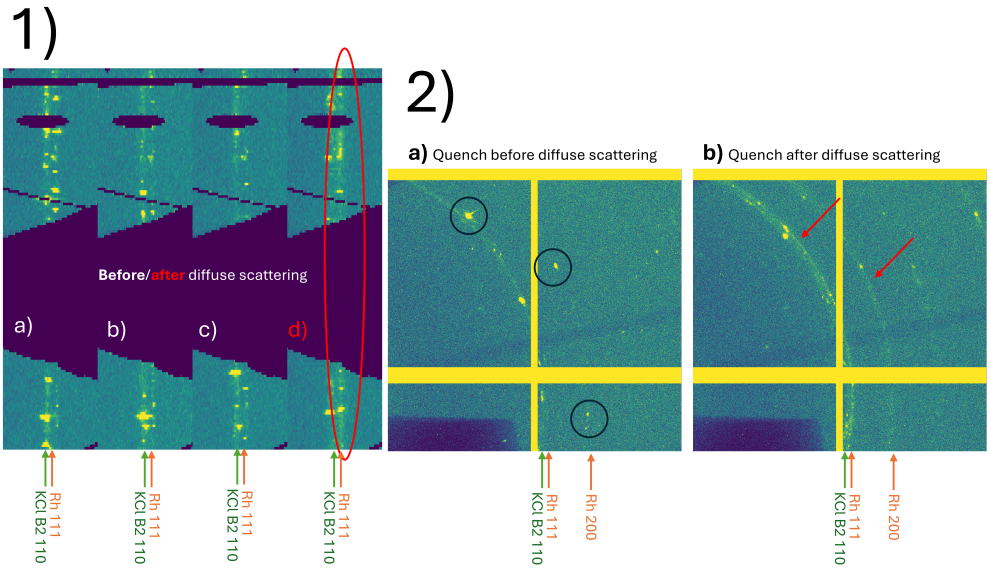

Figure S3 Left) Azimuthally unwrapped X-ray diffraction images of quenched rhodium at ∼100 GPa. (a)–(c) Samples quenched from temperatures below the onset of diffuse scattering, showing grainy and discontinuous Rh diffraction features indicative of grain growth. (d) Sample quenched after the appearance of diffuse scattering, exhibiting continuous Rh diffraction features characteristic of a fine-grained microstructure. **Right)** Selected regions of 2D X-ray diffraction images of quenched rhodium. (a) Example prior to the observation of diffuse scattering, with large, well-defined Rh diffraction spots (black circles). (b) Example after diffuse scattering, showing the emergence of continuous Debye rings and the disappearance of discrete diffraction spots, indicating melting during the preceding heating stage.

After the observation via *in situ* X-ray of diffuse scattering, a fine-grained texture and continuous Debye rings are observed in the quenched images, in contrast to the more single-crystal-like spots present at lower temperatures. Figure S3 shows representative examples at ∼100 GPa. While the *in situ* diffuse scattering indicates that either KCl, Rh, or both may be molten during heating, quench analysis is required to unambiguously determine the origin of the diffuse signal.

The left panel of Fig. S3 presents a sequence of quenched cake images obtained at different heating stages. The rightmost image corresponds to the quench following the appearance of a diffuse ring at ∼5000 K. A clear transition in texture is observed: earlier quenches show features consistent with grain growth, whereas the post-melting quench exhibits a fine-grained microstructure. The right panel further illustrates this transition through selected 2D diffraction images. Together, these observations provide unambiguous confirmation that diffuse scattering originates from molten rhodium.

5 MELTING SIMULATIONS

Our quantum molecular dynamics (QMD) melting simulations were carried out using the Z method implemented with VASP. The Z-method is a procedure for the calculation of the melting curves of materials by modeling a solid system at different initial total energies. The idea of the method was put forward by Belonoshko *et al.* in Ref.[6]. A solid system is modeled in a NVE ensemble (N is the number ot atoms, and V and E are the volume and total energy of the system, respectively). In each simulation E is controlled by the corresponding choice of the initial T. Essentially, the Z method simulates a solid in a superheated limit. The solid will melt spontaneously if the simulation is long enough, and T will drop to T_m (at $P = P_m$.) The shape of the P-T trajectory mapped out by the final states of simulations with different initial Ts resembles the letter Z, which is how the method got its name. After the original study of melting (of Pb) in the limit of solid supereating [7], the method has evolved into a well established scientific methodology. In fact, the Z method has been used in numerous studies of melting curves, e.g., of Fe and Fe-Si alloy [8], Zn [9], Sn [10], and Pt [11], just to name a few. The practical implementation of the Z method can be found in Refs.[6, 12, 13].

We have obtained the theoretical melting curve of fcc-Rh using the Z method implemented with VASP, as discussed above. For our study we used a 500-atom ($5\times5\times5$) supercell. For such a large system, full energy convergence, to $\lesssim$ 1 meV/atom, was achieved already with a single Γ-point, as our tests clearly demonstrate. A time step of 1 fs was used. Runs of as long as 30000 time steps, or 30 ps, were carried out. We simulated eight melting points of fcc-Rh, by performing an average of five computer runs per point (for a total of $\sim$ 40 computer runs). Our results are summarized in Table S4. The errors in melting T (T_m) are half of the increment of the initial T for a series of computer runs at the corresponding density [13]. We chose these increments to be 250 K for the first, 312.5 K for the second, 500 K for the third, 625 K for both the fourht and fifth, 750 K for the sixth, 1000 K for the seventh, and 1250 K for the eighth point, in the order of increasing density. The corresponding T_m errors are listed in Table S4 as ΔT_m. The errors in melting P (P_m) are negligibly small, of order 1-2 GPa in each case.

lattice constant (Å)	density (g/cm^3)	P_m (GPa)	T_m (K)	ΔT_m (K)
4.000	10.680	-18.6	1110	125.0
3.800	12.457	24.5	3210	156.3
3.650	14.056	80.6	4820	250.0
3.500	15.942	172	6730	312.5
3.375	17.859	297	8770	312.5
3.250	19.911	492	11330	375.0
3.150	21.868	727	13860	500.0
3.075	23.508	970	16110	625.0

Table S4 Eight *ab initio* melting points of fcc-Rh, $(P_m, T_m \pm \Delta T_m)$, obtained using the Z-method implemented in VASP.

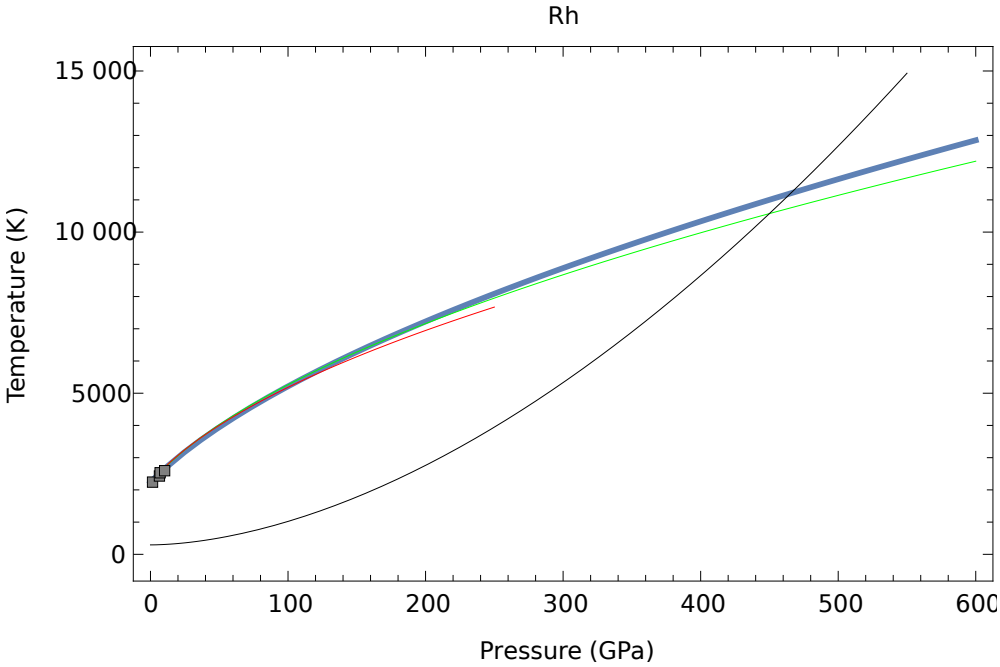

Figure S4 The melting curve of Rh: comparison of the QMD results of this work described by Eq. (1) (blue curve) to the low-P experimental data of Ref. [17] (boxes) as well as the theoretical results of Refs.[15] and [16] (green and red curves, respectively).

The best fit of the Simon-Glatzel form ($T_m(P) = T_m(0)(1 + P/a)^b$) to the eight QMD datapoints of Table represents the corresponding melting curve:

$$T_m^{\mathrm{fcc-Rh}}(P) = 2237.0 \left(1 + \frac{P}{25.7}\right)^{0.54}, \qquad (1)$$

which is our theoretical melting curve of rhodium. For this melting curve, the initial slope is 47.0 K/GPa, in excellent agreement with the thermodynamically based 45 ± 16 K/GPa [14]. In Fig. this melting curve is compared to another two theoretical melting curves of Rh available in the literature, namely, those of Refs. [15] and [16]. Fig. also shows the principal Hugoniot of Rh that we calculated (T in K, P in GPa): $T_H(P) = 293 + 0.22 \cdot P^{1.76}$. The Hugoniot crosses the melting point at $(P, T) =$ (465 GPa, 11200 K) which is the shock melting point of Rh. Note that our value is in excellent agreement with (470 GPa, 10800 K) of Ref.[15].

6 THERMAL EQUATION OF STATE OF LIQUID Rh

For the calculation of the thermal equation of state (EOS) of liquid Rh, we used liquid configurations which resulted in our QMD Z-method runs. In other words, we used

liquid configurations of 500 atoms in a cubic computational box. Since the PBEsol implementation of DFT is intended for the application to solids but presumably not to liquids, its PBE implementation was used instead. Direct comparison of the results produced using PBE, PBEsol, and several other DFT implementations such as AM05 (Armiento-Mattsson for GGA) revealed that indeed PBE outperforms all the rest. More specifically, with the use of PBE, the equilibrium density (ρ) of liquid Rh at the ambient melting point turns out to be 10.72 g/cm^3, in essential agreement with 10.82 ± 0.22 g/cm^3 from experiment [18], while the values which result from using different DFT implementations appear to be further away. Note that the value of $\rho(P = 0)$ (that is, $\rho(T_m = 2236$ K) that comes from the interpolation of the melting data in Table is 10.54 g/cm^3. A 1.5% difference between 10.54 and 10.72 must come from the fact that the melting data in Table are obtained using PBEsol while 10.72 is based on PBE.

The finite-T simulations of the thermal equation of state (EOS) were carried out using the algorithm of Nosé (SMASS=0 in VASP) in which during a QMD run with fixed volume (or fixed density, ρ) both T and P undergo controlled oscillations around, respectively, T chosen for the run and equilibrium $P_{\rm eq}$ the value of which is assigned to the corresponding (ρ, T). For these simulations, used liquid configurations which resulted in our QMD Z-method runs. In other words, we used liquid configurations of 500 atoms in a cubic computational box. As before, a single Γ-point was used. We performed 5 QMD runs at a series of fixed T from 3000 K to 5000 K with an increment of 500 K at 5 different system volumes that correspond to $P \sim 0 - 100$ GPa, and 5 QMD runs at a series of fixed T from 5000 K to 7000 K with an increment of 500 K at 5 different system volumes that correspond to $P \sim 100 - 250$ GPa, for a total of 50 QMD runs of liquid Rh. The duration of each of the 50 runs was 15000 time steps with a time step of 1 fs, that is, 15 ps. In QMD runs performed for the calculation of radial distribution functions (RDFs) of liquid Rh at given (P, T), RDFs were dumped over the last 5000 time steps, or the last 5 ps of running time.

We assume that the thermal EOS is of the form

$$P(\rho, T) \,=\, P(\rho, T_{\rm ref}) \,+\, C\,(T - T_{\rm ref}), \tag{2}$$

where $T_{\rm ref}$ is a reference point which is convenient to choose to be the ambient $T_m =$ 2236 K. Typically, for a solid $C = (\alpha B_T)$, where α and B_T are, respectively, the thermal expansion coefficient and isothermal bulk modulus the product of which is assumed to be independent of T. For liquid, we do not associate C with the product αB_T but consider it as a free parameter the value of which comes from fitting the above functional form to the data, either experimental or numerical, or both. Fitting the results of our calculations (using PBE) with the 3rd-order Birch-Murnaghan (BM3) EOS of the form (in the following B and B' stand for bulk modulus (in GPa) and its pressure derivative, respectively, and the subscript m means $(T = T_m,\, P = 0)$)

$$P(\rho, T_m) \,=\, \frac{3}{2}\, B_m \left(\eta^{7/3} \,-\, \eta^{5/3}\right) \left[1 \,+\, \frac{3}{4}\,(B'_m - 4)\left(\eta^{2/3} \,-\, 1\right)\right], \tag{3}$$

where $\eta \equiv \rho/\rho_m$, results in the following sets of parameters for liquid fcc-Rh:

$$\rho_m = 10.72 \text{ g/cm}^3, \quad B_m = 142.5 \text{ GPa}, \quad B'_m = 5.6, \quad C = 8.5 \cdot 10^{-3} \text{ GPa K}^{-1}.$$

7 LIQUID RHODIUM ANALYSIS

The structure of liquid rhodium was analysed using the AMORPHEUS Python code[19] in order to extract the radial distribution function $g(r)$ and atomic density at three different P-T conditions. Specifically the XRD signal from the liquid $I_{\text{sample}}(Q)$ was obtained by substracting the last XRD solid image before melting $I_{\text{bkg}}(Q)$ to the one that contains the signal from the liquid $I_{\text{meas}}(Q)$. Masks were applied using DIOPTAS [20] in order to remove, as much as possible, the signal from the solid phases present in the XRD patterns. The data were subsequently processed using the RPS functionality implemented in AMORPHEUS, which allows peak removal [19]. Then the sample's signal was obtained by removing the contribution from the environment as $I_{\text{sample}}(Q) = I_{\text{meas}}(Q) - b * I_{\text{bkg}}(Q)$. b is a factor for the background correction, an adimensional parameter that was optimized during the analysis. The structure factor $S(Q)$ and $F(r)$ were obtained from the $I_{\text{sample}}(Q)$. The density of the liquid and $g(r)$ were obtained by minimizing the figure of merit $\chi^2(r_{min}, b, Q_{max}, \rho) = \int_0^{r_{min}} [\Delta F(r)]^2 dr$ i.e. minimization at a low distance on the obtained X-ray weighted radial distribution function. The global analysis is performed after 5 iterations, for the removal of the noise at lowr. Final $g(r)$ is obtained by applying a Lorch modification function. The data shown here were obtained using Q_{max} values between 60 and 80 nm^{-1}. In order to obtain the most reliable values, the experimental $g(r)$ functions were compared with those simulated using the PBE functional. The results are shown in Fig.S5. It can be seen that the experimental analysis led to a good minimization, since $g(r)$ approaches zero for $r < r_{\text{min}}$. In addition, the experimental radial distribution functions reproduce the simulated ones to a reasonable extent. The largest discrepancy is observed for the radial distribution function at 39 GPa.

Uncertainties in the density determination arise from several factors. The effect of Q_{max} was also investigated in order to estimate the associated errors in the determined density. Truncation effects for Q_{max} values around 70–80 nm^{-1}, which are typical for LH-DAC experiments and correspond to the values used here, are limited to within ± 2.0 atoms/nm^3 [21].

The atomic density is also highly sensitive to the choice of r_{min}. The reliability of the obtained r_{min} values can be assessed through analysis of the pair correlation function, since this parameter should coincide with the onset of the first coordination shell in $g(r)$, which is fulfilled in our case (see Fig.S5). Typical uncertainties of ± 3 atoms/nm^3 are generally assigned for LH-DAC experiments with $Q_{\text{max}} < 80$ nm^{-1} [21]. In this experiment we have assigned values of errors for the density of $\pm 3 - 4.5$ atoms/nm^3 by inspection of the figure of merit χ^2 as a function of the mentioned parameters r_{min}, b, Q_{max}.

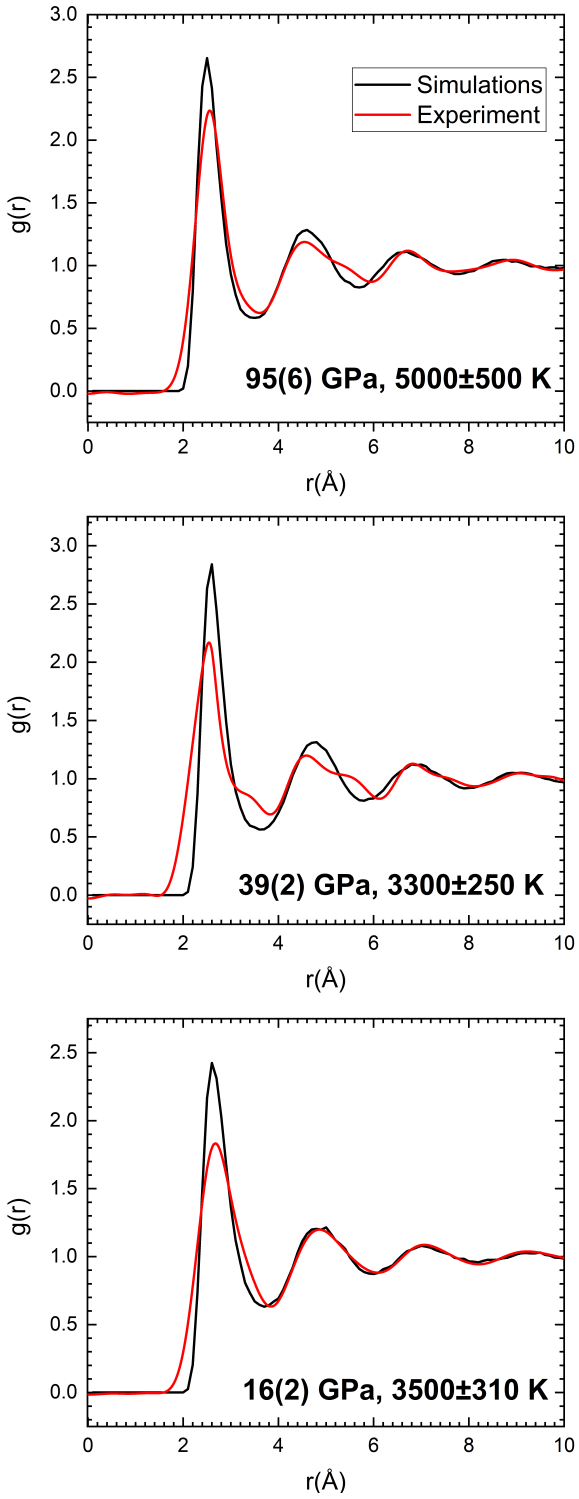

Figure S5 Radial distribution functions obtained at three different P-T conditions for liquid Rh compared with the simulated ones using PBE

8 TEMPERATURE MEASUREMENTS

The LH-DAC experiments were performed using laser-heating (LH) systems installed at the extreme conditions beamlines I15 at Diamond Light Source and ID27 at ESRF. A detailed description of the I15 setup is provided in Anzellini *et al.* [22], while the ID27 system is described in Mezouar *et al.* [23]. For completeness, schematic representations of both systems are shown in Supplementary Figures S6 and S7.

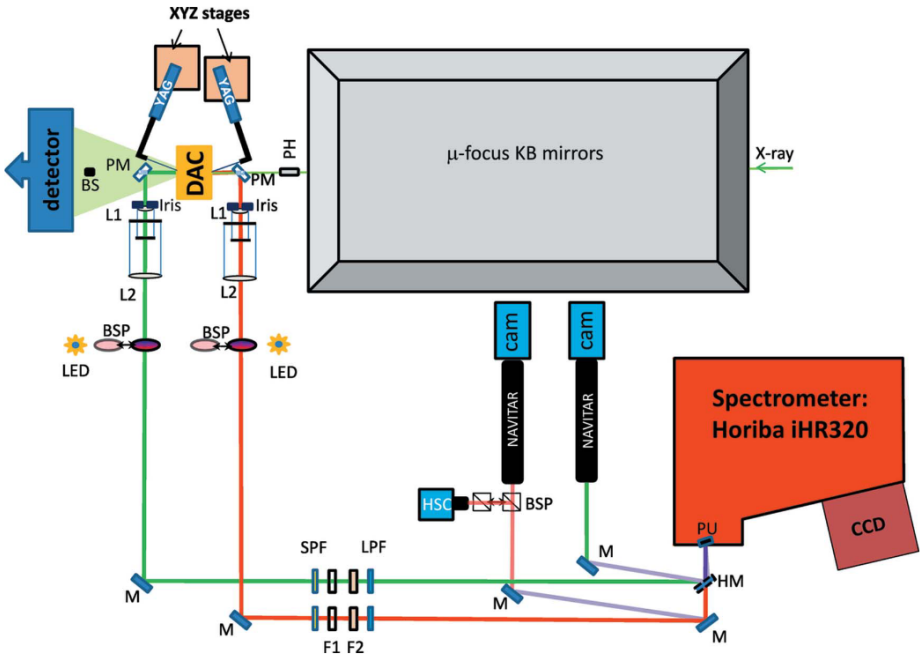

Figure S6 Schematics of the laser-heating system used on the I15 beam- line: Red and green lines represent the down and up-stream optical paths, respectively. The various components abbreviations are as follows: BS: beam-stop; L: lens; YM: YAG mirror; PH: pinhole; PM: Perforated mirror; BSP: Removable beam-splitter for LED illumination of the sample; M: mirror; SPF: Short-pass filter; LPF: Long-pass filter; F1 and F2: Neutral density filters; HM: Half mirror; PU: perforated mirror at the entrance of the spectrometer. Image extracted from [22]

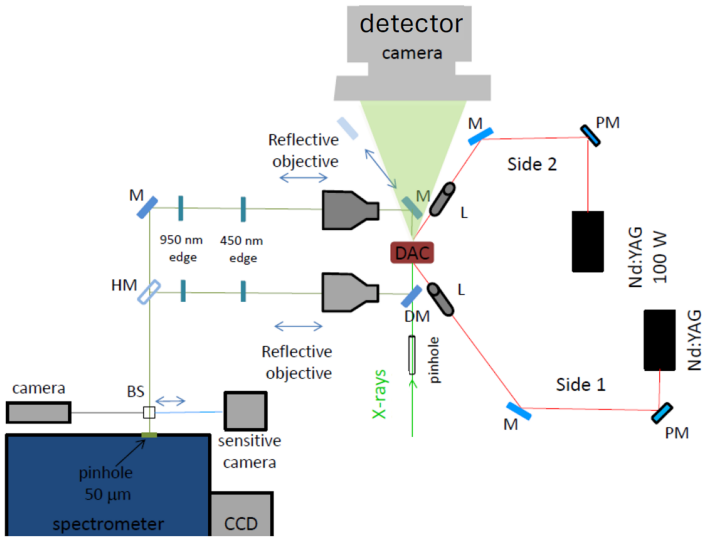

Figure S7 Schematic of the experimental setup of the beamline ID27 as reported in the PhD thesis S. Anzellini[24] In the figure M: Mirror, PM: polarizes mirror, HM: half mirror, L: lens

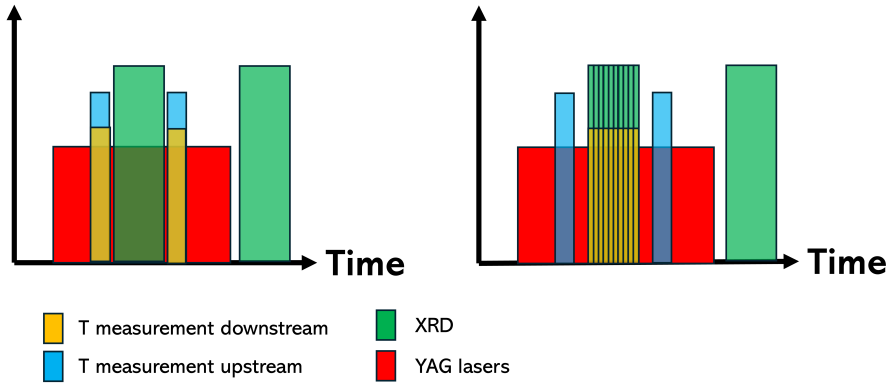

Figure S8 Schematic comparison of the data acquisition protocols. **Left**: Standard "trigger mode" at Diamond Light Source. **Right**: Modified protocol implemented at the ID27 beamline (ESRF).

In these experiments, temperature was determined using spectral radiometry. Thermal emission from the sample surface was collected through either refractive or reflective optics, depending on the configuration, and focused onto the entrance slit of an optical spectrometer. The optical path was calibrated using a tungsten lamp as a temperature standard, after which the thermal radiation emitted by the laser-heated hotspot was recorded.

Temperature determination in diamond anvil cell experiments via spectroradiometry can involve significant uncertainties, particularly at very high temperatures. The main source of error arises from the unknown wavelength dependence of the sample emissivity; in this work, emissivity is assumed to be constant (gray-body approximation). Additionally, due to the Gaussian temperature distribution of the laser-heated spot, the collected signal may represent a contribution of different local temperatures.

To account for these uncertainties, temperature errors were evaluated by comparing Planck fits with two-color pyrometry fits, following the approach described by Benedetti and Loubeyre [25]. Temperatures were extracted from Planck fits within a wavelength range ≥ 250 nm, where the two-color signal is approximately constant (see Figure S9).

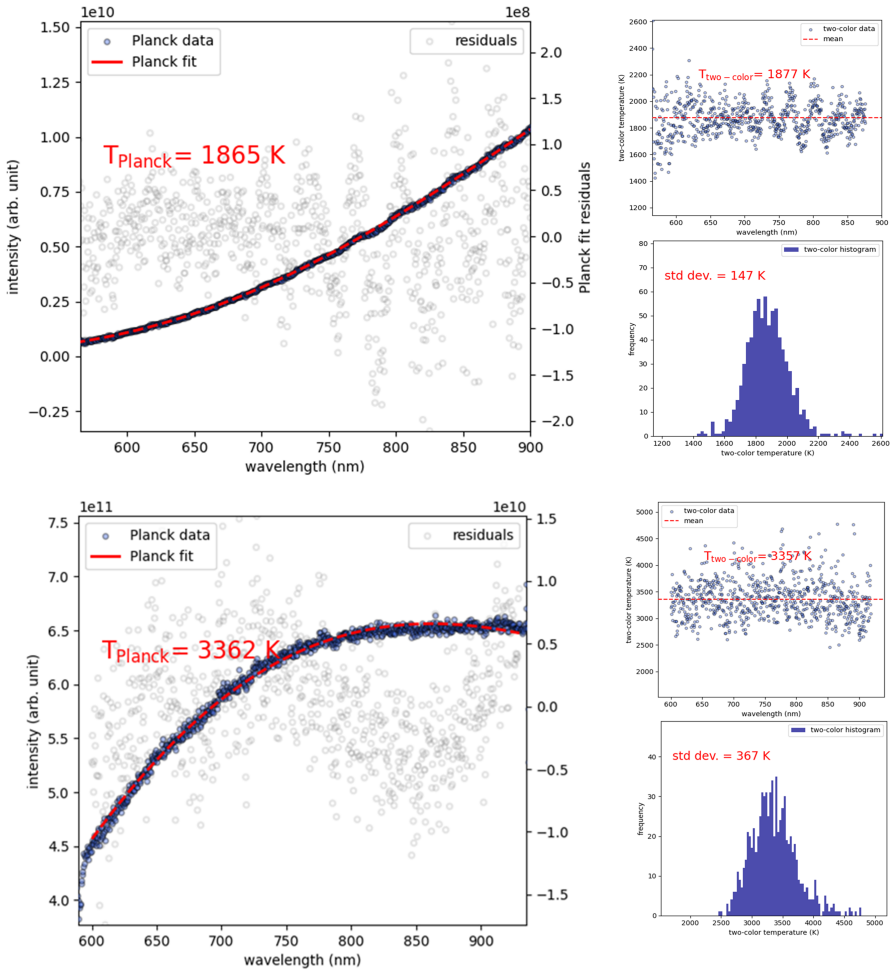

Figure S9 Example of Planck fit, in red, at 1865 K and 3362 K. In the right panel the two color fits are shown with the mean temperature in red dashed line. The histograms represent the variance of the distribution of temperatures around the mean value in the two-color plot.

For each heating step (i.e., constant laser power), the temperature was calculated as the average of all valid measurements. Individual measurement uncertainties were estimated as the standard deviation obtained from the two-color fit. The final uncertainty assigned to each heating step corresponds to the larger value between: (i) the standard deviation of the two-color fits, and (ii) the spread between individual temperature measurements.

To further assess the reliability of the temperature measurements, the temporal stability of the system was analyzed for the ESRF experiments. For each measurement, two upstream (*ex situ*) and ten downstream (*in situ*) temperature readings were collected. For each heating ramp and step, the mean temperature T_{mean} was calculated using all valid measurements (excluding those affected by detector saturation or poor signal quality). The temperature variation within each step, ΔT, was defined as the difference between the maximum and minimum recorded temperatures.

The temperature difference ΔT (typically 50–100 K) is generally smaller than the uncertainty associated with the two-color fit (150-500K) at lower temperatures (up to 2500 K approximately), as shown in Figure S10. As expected, the difference increases with temperature. While at lower temperatures we observe that the temperature variation within different short time measurements is extremely small it increases as we reach higher T's, specifically about 3000 K, this could be due to changes in the pressure transmitting medium thermal conductivity or changes in the emissivity of the metal studied at high temperature.

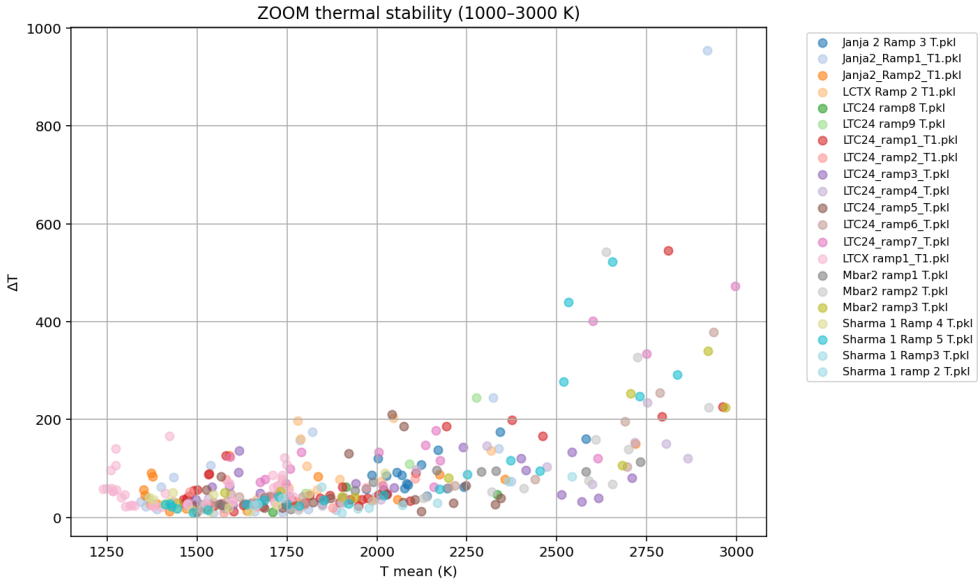

Figure S10 Temperature difference ΔT versus mean temperature for different LH heating ramps up to 3000 K.

References

[1] Dorogokupets, P.I.: P–v–t equations of state of mgo and thermodynamics. Physics and Chemistry of Minerals **37**(9), 677–684 (2010) https://doi.org/10.1007/s00269-010-0367-2

[2] Wakisaka, T., Kusada, K., Wu, D., Yamamoto, T., Toriyama, T., Matsumura, S., Akiba, H., Yamamuro, O., Ikeda, K., Otomo, T., Palina, N., Chen, Y., Kumara, L.S.R., Song, C., Sakata, O., Xie, W., Koyama, M., Kubota, Y., Kawaguchi, S., Arevalo, R.L., Aspera, S.M., Arguelles, E.F., Nakanishi, H., Kitagawa, H.: Rational synthesis for a noble metal carbide. Journal of the American Chemical Society **142**(3), 1247–1253 (2020) https://doi.org/10.1021/jacs.9b09219

[3] Dewaele, A., Mezouar, M., Guignot, N., Loubeyre, P.: High melting points of tantalum in a laser-heated diamond anvil cell. Phys. Rev. Lett. **104**, 255701 (2010) https://doi.org/10.1103/PhysRevLett.104.255701

[4] Anzellini, S., Herlihy, A., Dominijanni, S., Botella, P., Brooks, A., Burakovsky, L., Pakhomova, A., Errandonea, D.: Phase diagram of ruthenium characterized in situ by synchrotron x-ray diffraction and ab initio simulations. Results in Physics **65**, 107961 (2024) https://doi.org/10.1016/j.rinp.2024.107961

[5] Hrubiak, R., Meng, Y., Shen, G.: Microstructures define melting of molybdenum at high pressures. Nature Communications **8**(1), 14562 (2017) https://doi.org/10.1038/ncomms14562

[6] Belonoshko, A.B., Skorodumova, N.V., Rosengren, A., Johansson, B.: Melting and critical superheating. Phys. Rev. B **73**, 012201 (2006) https://doi.org/10.1103/PhysRevB.73.012201

[7] Cricchio, F., Belonoshko, A.B., Burakovsky, L., Preston, D.L., Ahuja, R.: High-pressure melting of lead. Phys. Rev. B **73**, 140103 (2006) https://doi.org/10.1103/PhysRevB.73.140103

[8] Belonoshko, A.B., Rosengren, A., Burakovsky, L., Preston, D.L., Johansson, B.: Melting of fe and $fe_{0.9375}si_{0.0625}$ at earth's core pressures studied using ab initio molecular dynamics. Phys. Rev. B **79**, 220102 (2009) https://doi.org/10.1103/PhysRevB.79.220102

[9] Errandonea, D., MacLeod, S.G., Ruiz-Fuertes, J., Burakovsky, L., McMahon, M.I., Wilson, C.W., Ibañez, J., Daisenberger, D., Popescu, C.: High-pressure/high-temperature phase diagram of zinc. Journal of Physics: Condensed Matter **30**(29), 295402 (2018) https://doi.org/10.1088/1361-648X/aacac0

[10] Rehn, D.A., Greeff, C.W., Burakovsky, L., Sheppard, D.G., Crockett, S.D.: Multiphase tin equation of state using density functional theory. Phys. Rev. B **103**, 184102 (2021) https://doi.org/10.1103/PhysRevB.103.184102

[11] Burakovsky, L., Preston, D.L., Errandonea, D.: Ab initio study of randomly disordered hexagonal close-packed (rhcp) phase in platinum. Journal of Applied Physics **137**(1), 015109 (2025) https://doi.org/10.1063/5.0235811

[12] Burakovsky, L., Chen, S.P., Preston, D.L., Sheppard, D.G.: Z methodology for phase diagram studies: platinum and tantalum as examples. Journal of Physics: Conference Series **500**(16), 162001 (2014) https://doi.org/10.1088/1742-6596/500/16/162001

[13] Burakovsky, L., Burakovsky, N., Preston, D.L.: Ab initio melting curve of osmium. Phys. Rev. B **92**, 174105 (2015) https://doi.org/10.1103/PhysRevB.92.174105

[14] Arblaster, J.W.: Selected values for the densities and molar volumes of the liquid platinum group metals and of the initial melting curves of iridium, rhodium and ruthenium. Johnson Matthey Technology Review **61**(2), 80–86 (2017) https://doi.org/10.1595/205651317X694461

[15] Smirnov, N.A.: Ab initio calculations of structural stability, thermodynamic and elastic properties of ni, pd, rh, and ir at high pressures. Journal of Applied Physics **134**(2), 025901 (2023) https://doi.org/10.1063/5.0158737

[16] Tam, N.T., Lam, L.T., Hieu, H.K.: Investigation of equation-of-state and melting behavior of rhodium up to 200 gpa. Physics Letters A **543**, 130450 (2025) https://doi.org/10.1016/j.physleta.2025.130450

[17] Strong, H.M., Bundy, F.P.: Fusion curves of four group viii metals to 100 000 atmospheres. Phys. Rev. **115**, 278–284 (1959) https://doi.org/10.1103/PhysRev.115.278

[18] Paradis, P.-F., Ishikawa, T., Yoda, S.: Thermophysical property measurements of supercooled and liquid rhodium. International Journal of Thermophysics **24**(4), 1121–1136 (2003) https://doi.org/10.1023/A:1025065304198

[19] Boccato, S., Garino, Y., Morard, G., Zhao, B., Xu, F., Sanloup, C., King, A., Guignot, N., Clark, A., Garbarino, G., Morand, M., Antonangeli, D.: Amorpheus: a python-based software for the treatment of x-ray scattering data of amorphous and liquid systems. High Pressure Research **42**(1), 69–93 (2022) https://doi.org/10.1080/08957959.2022.2032032

[20] Prescher, C., Prakapenka, V.B.: Dioptas: a program for reduction of two-dimensional x-ray diffraction data and data exploration. High Pressure Research **35**(3), 223–230 (2015) https://doi.org/10.1080/08957959.2015.1059835

[21] Morard, G., Garbarino, G., Antonangeli, D., Andrault, D., Guignot, N., Siebert, J., Roberge, M., Boulard, E., Lincot, A., Denoeud, A., Petitgirard, S.: Density measurements and structural properties of liquid and amorphous metals under high pressure. High Pressure Research **34**(1), 9–21 (2014) https://doi.org/10.

1080/08957959.2013.860137

[22] Anzellini, S., Kleppe, A.K., Daisenberger, D., Wharmby, M.T., Giampaoli, R., Boccato, S., Baron, M.A., Miozzi, F., Keeble, D.S., Ross, A., Gurney, S., Thompson, J., Knap, G., Booth, M., Hudson, L., Hawkins, D., Walter, M.J., Wilhelm, H.: Laser-heating system for high-pressure x-ray diffraction at the extreme conditions beamline i15 at diamond light source. Journal of Synchrotron Radiation **25**(6), 1860–1868 (2018) https://doi.org/10.1107/S1600577518013383

[23] Mezouar, M., Garbarino, G., Bauchau, S., Morgenroth, W., Martel, K., Petitdemange, S., Got, P., Clavel, C., Moyne, A., Kleij, H.-P.V.D., Pakhomova, A., Wehinger, B., Gerin, M., Poreba, T., Canet, L., Rosa, A., Forestier, A., Weck, G., Datchi, F., Wilke, M., Jahn, S., Andrault, D., Libon, L., Pennacchioni, L., Kovalskii, G., Herrmann, M., Laniel, D., Bureau, H.: The high flux nano-x-ray diffraction, fluorescence and imaging beamline id27 for science under extreme conditions on the esrf extremely brilliant source. High Pressure Research **44**(3), 171–198 (2024) https://doi.org/10.1080/08957959.2024.2363932

[24] Anzellini, S.: Phase diagram of iron under extreme conditions measured with time resolved methods. Ph.d. thesis, Université Pierre et Marie Curie-Paris VI, Paris, France (2014)

[25] Benedetti, L.R., Loubeyre, P.: Temperature gradients, wavelength-dependent emissivity, and accuracy of high and very-high temperatures measured in the laser-heated diamond cell. High Pressure Research **24**(4), 423–445 (2004) https://doi.org/10.1080/08957950412331331718